The cascading foreshock sequence of the *Ms* 6.4 Yangbi earthquake in Yunnan, China

Gaohua Zhu [a], Hongfeng Yang [a],*, Yen Joe Tan [a], Mingpei Jin [b], Xiaobin Li [b], Wei Yang [c]

[a] *Earth System Science Programme, Faculty of Science, The Chinese University of Hong Kong, Shatin, Hong Kong 999077, China*
[b] *Yunnan Earthquake Agency, Kunming 650224, China*
[c] *Key Laboratory of Seismic Observation and Geophysical Imaging, Institute of Geophysics, China Earthquake Administration, Beijing 100081, China*

ARTICLE INFO

ABSTRACT

Foreshocks may provide valuable information on the nucleation process of large earthquakes. The 2021 *Ms* 6.4 Yangbi, Yunnan, China, earthquake was preceded by abundant foreshocks in the ~75 hours leading up to the mainshock. To understand the space-time evolution of the foreshock sequence and its relationship to the mainshock nucleation, we built a high-precision earthquake catalog using a machine-learning phase picker—EQTransformer and the template matching method. The source parameters of 17 large foreshocks and the mainshock were derived to analyze their interaction. Observed "back-and-forth" spatial patterns of seismicity and intermittent episodes of foreshocks without an accelerating pattern do not favor hypotheses of pre-slip in the nucleation region of the mainshock. The ruptured patches of most large foreshocks were adjacent to one another with little overlap, and the mainshock eventually initiated near the edge of the foreshocks' ruptured area where there had been a local increase in shear stress. These observations are consistent with a triggered cascade of stress transfer, where previous foreshocks load adjacent fault patches to rupture as additional foreshocks, and eventually the mainshock.

© 2022 Elsevier B.V. All rights reserved.

1. Introduction

Foreshocks have been considered promising precursors to examining how earthquakes nucleate and grow (Bouchon et al., 2013; Ellsworth and Bulut, 2018; Huang et al., 2020; Kato and Ben-Zion, 2020; Kato et al., 2012). However, it is in debate which physical mechanism, pre-slip (deterministic perspective) or cascade triggering (stochastic perspective), dominantly contributes to foreshock sequences and mainshock nucleation processes (Gomberg, 2018; Ellsworth, 2019). In the preslip model, aseismic slip is expected to occur at the location of the mainshock hypocenter, driving foreshock sequences during the nucleation phase of the mainshock (Rubin and Ampuero, 2005; Tape et al., 2018). In comparison, the cascade model proposes that foreshocks are triggered by event-to-event stress transfer without aseismic slip (Ellsworth and Bulut, 2018; Yoon et al., 2019).

Debate continues over the two-end-member mechanisms, especially for a few reported foreshock sequences of intraplate earthquakes. Dodge et al. (1996) suggested that foreshocks of the 1992 *Mw* 6.1 Joshua Tree earthquake caused negative Coulomb stress

distribution at the mainshock hypocenter, hence the mainshock is more likely a byproduct of an aseismic nucleation process. In contrast, Mori (1996) estimated the slip area of the largest foreshock of the 1992 *Mw* 6.1 Joshua Tree earthquake and found that the mainshock hypocenter is located outside the foreshock's rupture zone where there is stress increase, hence the foreshock sequence is compatible with the cascade model (Mori, 1996). For the 1999 *Mw* 7.1 Hector Mine foreshock sequence, an external aseismic transient (Chen and Shearer, 2013) or a cascade of stress transfer (Yoon et al., 2019) have both been proposed. Furthermore, for the 1999 *Mw* 7.6 Izmit foreshocks, the existence of aseismic slip driving the foreshocks is suggested by repeating events (Bouchon et al., 2011), whereas Ellsworth and Bulut (2018) argued that the "repeating" foreshocks are actually neighboring events, therefore indicating a stress-transfer–driven cascade of the sequence. Recently, a combination of aseismic transients and static stress transfer is suggested by the study of foreshock migration preceding the 2016 *Mw* 7.0 Kumamoto earthquake (Kato et al., 2016) and the 2019 *Mw* 7.1 Ridgecrest foreshock sequence (Huang et al., 2020).

Such debate stems from precision of earthquake locations and subsequent interpretations. Investigating the temporal and spatial evolution of foreshock sequences at high resolution may shed light on the key issue. On May 21, 2021, a *Ms* 6.4 earthquake occurred in Yangbi, Dali City, Yunnan Province, China, with a strike-slip fault-
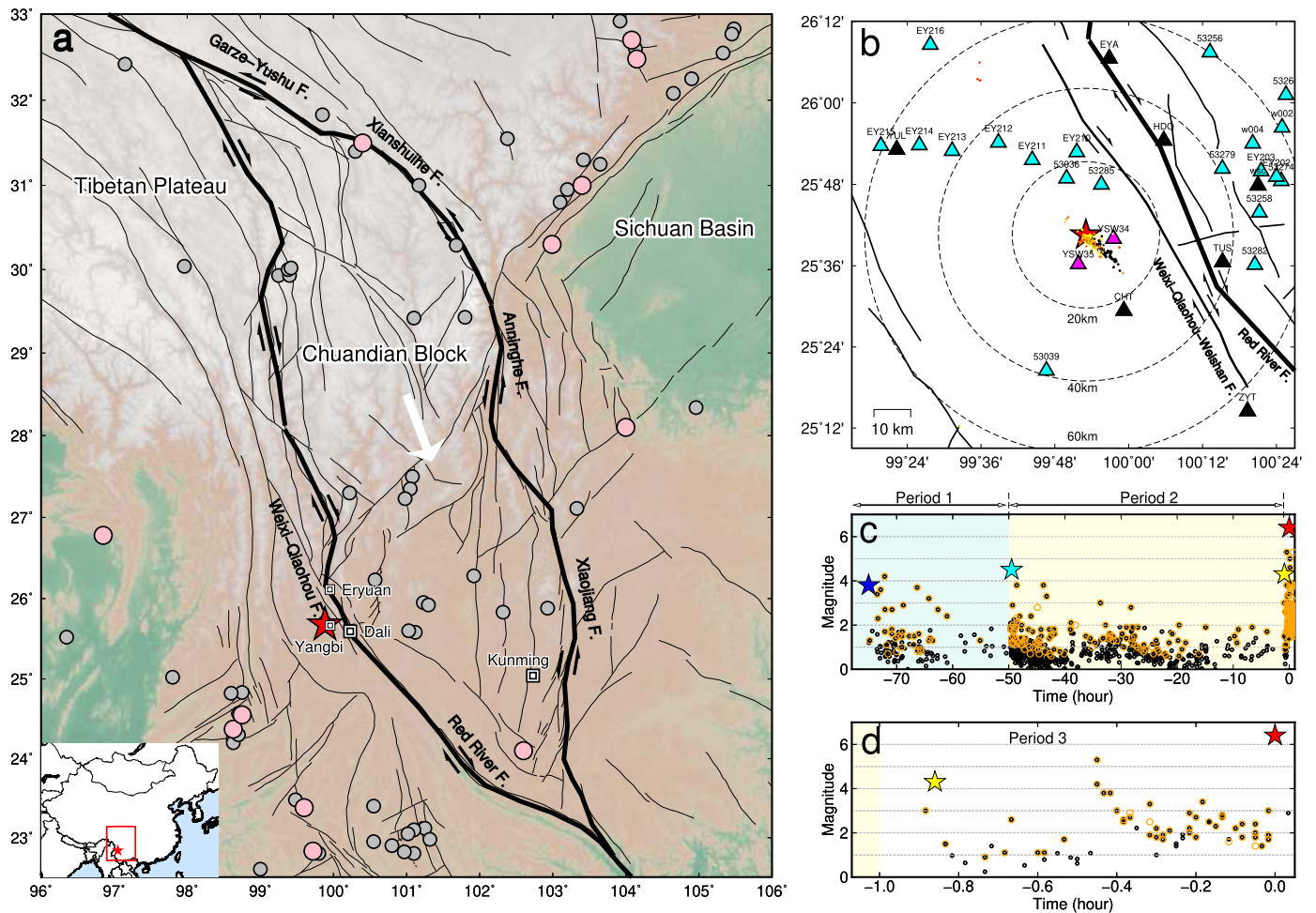
Fig. 1. (a) The tectonic map and historical large earthquakes surrounding the study region. The red star marks the hypocenter of the 2021 *Ms* 6.4 Yangbi mainshock (May 21st, 2021). The pink and gray dots represent $M_S \geq 7.0$ and $6.0 \leq M_S$ <7.0 historical earthquakes, respectively. **(b)** The seismic stations (triangles) and foreshock sequence (small dots colored by time) near the Weixi-Qiaohou-Weishan (WQW) Fault. The black and cyan triangles represent the permanent stations and the air gun source array, respectively. The two fuchsia triangles show the temporary seismic stations deployed ∼1 day before the mainshock. **(c, d)** Magnitude V.S. Time of foreshock sequence starting from May 18th, 2021, about 75 hours prior to the *Ms* 6.4 mainshock. The 3 windows of Period 1, 2 and 3 are colored based on the observations that the foreshock sequence appeared to be clustered temporarily. The blue, cyan, and yellow stars mark the first event of each period. The orange and black circles represent the catalog events and our detected and located events, respectively. (For interpretation of the colors in the figure(s), the reader is referred to the web version of this article.)

ing mechanism. The intensity of seismic activity started to increase significantly on May 18th, 3 days before the mainshock, including a *Ms* 5.3 event shortly preceding the M_S 6.4 Yangbi earthquake (Fig. 1c and 1d). This extensive foreshock sequence contributed to mitigating the mainshock's impact. Residents had stayed in tents or outside vulnerable buildings on May 20th, which helped reduce the number of casualties. Based on seismic recordings of permanent stations in tens to hundreds of kilometers, several studies suggest diverse mechanisms driving the foreshock sequence, e.g. cascade triggering (Zhang et al., 2021b; Yang et al., 2021b) or fluid flow (e.g. Lei et al., 2021; Su et al., 2021). Temporary seismic stations had been installed within 5 km of the mainshock rupture plane on May 20th (Fig. 1b), ∼1 day before the mainshock, therefore the near-field seismic observations provide a good opportunity to investigate how the foreshock sequence evolved.

Here we collect continuous data from both near-field temporary and permanent stations and use machine-learning and template matching methods to detect foreshocks. We then accurately locate detected earthquakes and calibrate their magnitude as well as derive focal mechanisms and source parameters (corner frequency, stress drop and source dimension) of the large ones. Then, by analyzing the temporal and spatial evolution of foreshocks and the

interaction of large foreshocks and mainshock, the mechanism of mainshock nucleation is discussed.

2. Tectonic setting and seismic network

Numerous faults are formed in southwestern China to accommodate the eastward escape of the Tibet Plateau associated with the collision of the Indian and Eurasian plates (Shen et al., 2005; Allen et al., 1984; Shi et al., 2018). Among these faults, the ∼1000-km-long Red River fault is a profound structural discontinuity, which is regarded as a west boundary of the Chuandian block (Fig. 1a). The Red River fault is characterized by a low slip rate of ∼0.4-2 mm/year evidenced by GPS observations (Wang et al., 2008) and stratigraphic and geomorphologic investigations (Shi et al., 2018). Faults with low slip rates can still produce catastrophic earthquakes, such as the 2008 *Mw* 7.9 Wenchuan, China earthquake (>80,000 deaths) that occurred along the slow-slipping Longmen Shan fault system (Shen et al., 2009). Nine damaging earthquakes were discovered close to the Dali-Eryuan region since C.E. 886 (Shi et al., 2018). Therefore, a large population in the region are at risk of great seismic hazard.

The 2021 *Ms* 6.4 Yangbi sequence near Dali city is located ∼15 km to the southwest of the Weixi-Qiaohou-Weishan (WQW) fault, the nearest mapped fault which is considered as induced by the

northward extension of the Red River Fault (Fig. 1a). Because of the well-known regional seismic hazard in the region, there are many existing seismic networks. China Earthquake Administration (CEA) has launched the China Array project and deployed permanent stations with a spacing of ∼40-60 km since 2011 (black triangles in Fig. 1b). Moreover, to monitor temporal variations of subsurface structure (Liu et al., 2021; Yang et al., 2021a; Luan et al., 2022), an air gun source that can repeatedly release large-volume compressed air was constructed in the Binchuan basin, Yunnan since April 2011 (Wang et al., 2012; Yang et al., 2020). After the operation of the air gun source in Yunnan, intermediate-period seismic stations (Guralp CMG-40 T) have also been deployed to complement the permanent seismic network (cyan triangles in Fig. 1b), some of which well covered the 2021 earthquake rupture.

Importantly, due to the sudden increase of seismicity on May 18th, temporary seismic stations within ∼5 km to the sequence have been installed by Yunnan Earthquake Administration on May 20th to monitor the earthquakes (fuchsia triangles in Fig. 1b). In this study, we collected continuous data from 26 stations within 60 km of the epicentral area, starting from May 1st 2021, including 5 permanent broadband stations of the Chinese Seismic Network (CSN), 19 air-gun array stations of Dali Experiment Center, and the 2 temporary stations temporarily deployed ∼1 days before the Yangbi mainshock (Fig. 1b). All stations are equipped with seismometers with a sampling rate of 100 Hz.

3. Earthquake detection and locations

We first adopted EQTransformer (Mousavi et al., 2020), a deep-neural-network-based picker, for detecting earthquakes and picking their P- and S-arrival times (Fig. S1). Three-component seismograms with a sampling rate of 100 Hz and 30-s time segments, with 50% overlap between consecutive segments, were provided as input for EQTransformer. We only retained picks above the probability threshold of 0.1 for P- and S-phase and detection threshold of 0.2 for events. We then associated the phase picks with individual events using the Rapid Earthquake Association and Location package (REAL) (Zhang et al., 2019). Only events with at least 6 phases, including at least 2 P- and 2 S-phases were retained. The events were preliminarily located at the grid with the maximum number of seismic picks or the grid with the smallest travel time residual if multiple grids have the same number of picks.

We then applied the template matching method using the relocated foreshocks from Zhang et al. (2021b) and newly detected events as templates. A 1-20 Hz bandpass file was applied to both the template and continuous data. We used P (1 s before to 4 s after the arrival) and S waves (3 s before to 5 s after the arrival) signal windows on three channels to cross correlate with the continuous data (Yang et al., 2009; Peng and Zhao, 2009). A phase was detected if the cross coefficient exceeded 0.5 on one single station. We combined the detected phases and removed all duplicate detections if their detecting time overlap (i.e. within ±1 s). We then associated the phase picks using the REAL package with same parameters as the previous process.

We then located the associated events with at least 2 P- and 2 S-picks and 6 total picks with the Hypoinverse algorithm (Klein, 2002) using a 1D velocity model (Zhang et al., 2021b). Double-difference method (Waldhauser and Ellsworth, 2000) was then used to relocate the events, with a total of 621,098 $P-$ and 521,995 S-phase differential times built from phase picks. We also measured differential travel times by cross-correlating P and S waveforms of -1.0 to 1.5 s and -1.5 to 2.5 s, respectively (filtered at 1-20 Hz, with 100 Hz sampling rate) and obtained a total of 116,583 P- and 55,567 S-phase differential times with the cross-correlation coefficients larger than 0.6. Both pick-derived and

cross-correlation-derived differential times were then used for the relocation, with the minimum number of 8 for the differential time measurements per event pair and the maximum separation of 10 km. We adopted the bootstrapping method to compute the relative location errors, during which we relocated the events 200 times while resampling the differential travel times (Waldhauser and Ellsworth, 2000). The horizontal minor/major axes and vertical projections of the 95% confidence ellipsoids have median values of 102, 147 and 216 m in the east-west, north-south, and vertical directions, respectively (Fig. S2). To estimate relative location uncertainties of the 17 largest foreshocks and the mainshock, we also ran hypoDD in the singular value decomposition (SVD) mode. Location uncertainties were within the range of 21-47 m, 24-86 m, 105-736 m in E-W, N-S, and vertical directions (error bars in Fig. 6). The final relocated catalog contains 796 foreshocks with magnitude of -0.1-5.3 and b value of 0.55 (Fig. S3). The magnitude of newly detected event were estimated based on average amplitude ratio (R) of maximum vertical amplitudes between newly detected events and the nearest catalog event with a known magnitude (M_0) (Yang et al., 2009; Zhu et al., 2019).

$$M_{det} = M_0 + log_{10}(R) \qquad (1)$$

To search for possible repeating earthquakes, we also calculated the maximum cross-correlation coefficient (CC) between all waveform pairs for relocated events, with data processing steps similar to previous studies (Huang et al., 2020; Peng and Zhao, 2009). The 3-component seismograms were filtered with a frequency band of 1-20 Hz, starting from 2 sec before and 8 sec after the picked or theoretical P-wave arrival times. We defined the candidate repeater pairs with CC ≥ 0.95 on at least 3 stations and found no relocated event pair meeting the criteria. Noted that we did not find repeating earthquakes during such a relatively short period, but cannot deny the possibility of the existence of repeating earthquakes in the long term. Detecting potential repeating earthquakes in a much longer time window (e.g. several years) with long-term templates can be an interesting future topic to study the long-term slip behavior along the fault.

4. Spatiotemporal pattern of foreshocks

A total of 796 events with the magnitude of -0.1-5.3 were relocated, which was about a fourfold increase in the number of foreshocks than reported in the CEA catalog. The foreshock sequence revealed a complicated sequence of foreshocks, but no repeating earthquakes were observed according to our criteria in the period from May 1st to May 21st, 2021. Most foreshocks were located linearly on the southwestern side of the WQW fault (Fig. 1b). The foreshock sequence became intense starting from May 18th, which was ∼75 hours before the *Ms* 6.4 mainshock (Fig. 1c). Based on their apparent timings, we divided the ∼75-hour-long foreshock sequence into three periods (Figs. 1c & 1d). Based on their spatial pattern, we divided the mainshock ruptured fault into zone 1, 2, 3 from northwest to southeast, with reference to the M_L 3.8 and *Ms* 4.5 earthquakes (the first event during periods 1, 2, respectively) (Fig. 2a).

The first period (75-50 hours before mainshock) started with an M_L 3.8 foreshock (f1) that occurred ∼6.4 km southeast of the M_S 6.4 mainshock (Fig. 2a & Fig. 3a) on May 18th. Notably, the f1 event nucleated at a depth of ∼6.2 km, deeper than most subsequent events and mainshock (Fig. 2d). In the following 25 hours, the foreshocks ruptured zone 2 (a small area between 4-7 km to the mainshock). The seismicity front showed northwest migration towards the mainshock during the beginning 5 hours, propagating about 2 km along the fault toward the northwest (migration speed:
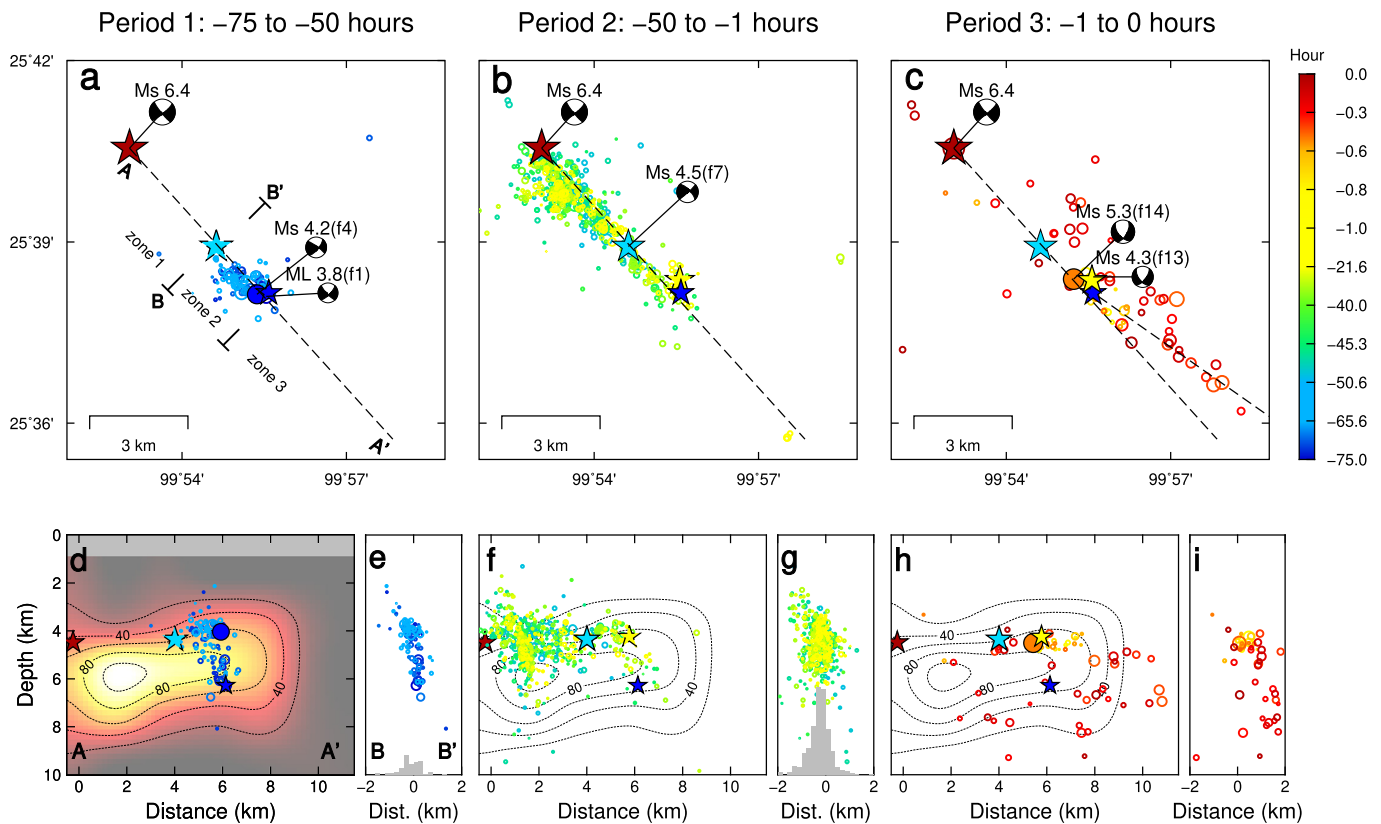
Fig. 2. Spatial-temporal evolution of the foreshock sequence colored by their original time relative to the M_S 6.4 mainshock (the dark red star) in three time periods: **(a)** -75 to -50 hours, **(b)** -50 to -1 hours, **(c)** -1 to 0 hours. The circle size is scaled by the magnitude. The blue, cyan, and yellow stars mark the first event of each period. The black dashed line represents the rupturing fault. **(d, f, h)** The fault-parallel cross-section of seismicity in each period. The background color and contours represent the slip of mainshock rupture (Guo et al., 2022). **(e, g, i)** The fault-perpendicular cross-section of seismicity in each period. The histograms in gray color show the distribution of event account.

9.6 km/d), but then the events stopped within zone 2. These events within zone 2 exhibited an apparent width of ~1 km on surface projection, delineated a nearly vertical fault plane (Figs. 2a, 2d, 2e). Note that the seismicity rate exhibited a significant increase immediately after the M_L 3.8 event, and then gradually decayed with time and became quiescent at the end of this period (-60 to -50 hours) (Fig. 3c).

The foreshock sequence became active again after the Ms 4.5 foreshock (f7) occurred at the northwest margin of zone 2 (Fig. 2b). Immediately following the Ms 4.5 event (within 0.2 hours), many smaller magnitude earthquakes were scattered promptly among the entire zone 1 (~4 km) (Figs. 2b, 3a, 3d). The period 2 sequence then mainly concentrated within 0-7 km to the mainshock, occupying both zone 1 and zone 2. Interestingly, the frequency of foreshocks in both zone 1 and zone 2 abruptly increased right after the Ms 4.5 event, but decayed with time after the event (Fig. 3c).

After a relatively quiescent period from -15 to -1 hour before mainshock, the events of the third period (-1-0 hour) ruptured back to the initial failure zone, starting with an Ms 4.3 foreshock (f13) that occurred close to the first M_L 3.8 earthquake (Fig. 2c & Fig. 3a). About 25 min later, an Ms 5.3 event (f14), the largest foreshock in this earthquake sequence struck the region. Immediately after the Ms 5.3 earthquake, scattered seismicity in zone 3 emerged (Fig. 2c & Fig. 3). 27 min after the largest Ms 5.3 foreshock, the mainshock ruptured initiating from the northwestern side of the fault and propagating towards the southeast (Lei et al., 2021). Most events during period 3 were located on a previously unknown branch fault at the southeastern end of the main fault or off the main rupture fault. Overall, the entire 75-hour-long foreshock sequence appeared to migrate to shallower depths at the initial phase (Fig. 2d and Fig. 6), and exhibited a northwest migra-

tion towards the mainshock during the beginning of period 1. Then foreshocks occurrence was intermittent within zone 1 and 2, then ruptured back to the initial failure zone and scattered during the final hour before the mainshock (period 3).

5. Focal mechanisms, rupture area and stress perturbations

To derive source parameters of the main foreshocks, we used all available local and regional stations within 400 km. Focal mechanism solutions of 3 largest foreshocks (f4, f7, f14) were derived from the Cut-And-Paste (CAP) method, and an additional 14 focal mechanism solutions of M > 2.8 foreshocks were determined with the HASH algorithm (Hardebeck and Shearer, 2002) using the P-wave polarity of at least 20 stations with an azimuthal gap less than 90° (Fig. S4). The source parameters of the 17 foreshocks (f1-f17) and the mainshock (m18) were listed in Table S1. We reconstructed the fault plane (Fig. S5) using the L1 norm to fit located events after removing obvious off-fault events (Yang et al., 2009). The best-fitting plane has a strike (134°) and dip (84°), consistent with those from available moment tensor solutions for the main events (strike=140°, dip=84°) (Fig. 4 and Fig. S6).

Most foreshocks and the mainshock hypocenter were located roughly linearly on the southwestern side of the WQW fault (Fig. 1b), delineating a SE-trending fault plane, consistent with the SE-trending nodal plane of the mainshock focal mechanism (Fig. 4). Although most foreshocks showed similar strike-slip faulting mechanisms with the mainshock, the largest Mw 5.2 foreshock (f14) and f13 exhibited different focal mechanisms with appreciable normal faulting components (Fig. 4). Moreover, Lei et al. (2021) suggest that the largest foreshock (f14) ruptured northeastward unilaterally on a northeast-trending conjugate fault (fault 3
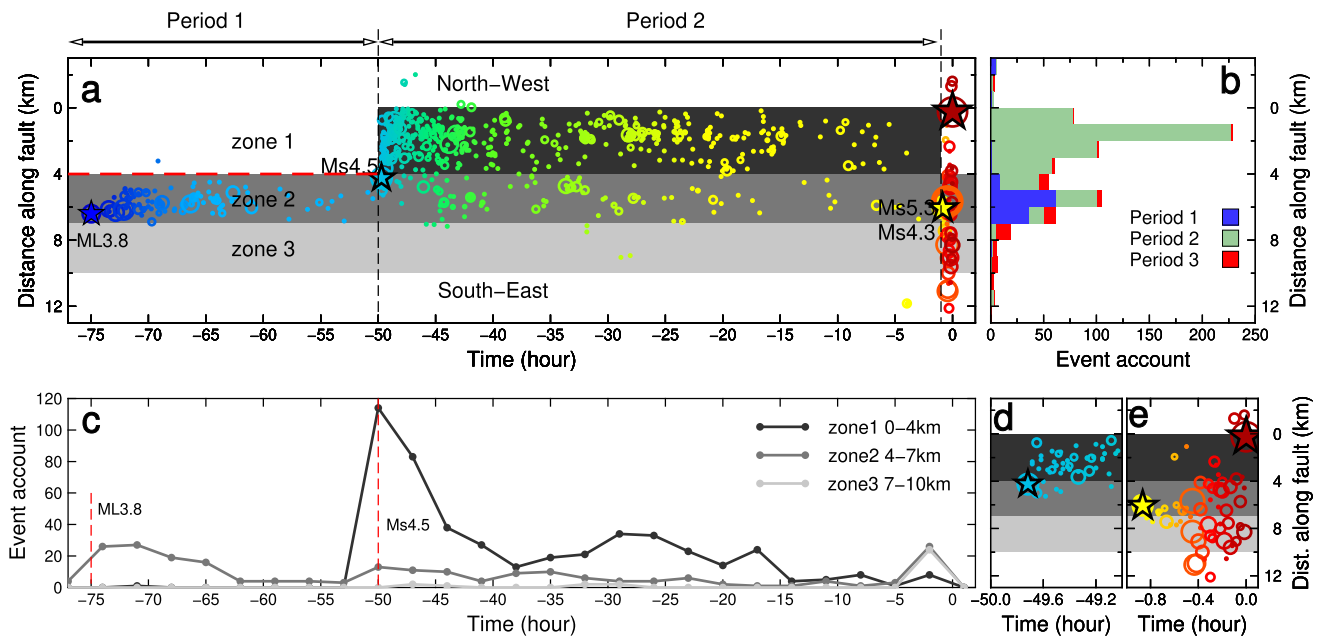
Fig. 3. (a) Space-time diagram of the foreshocks along fault strike distance. Distance is taken along the fault strike direction with 0 km corresponding to the hypocenter of the *Ms* 6.4 mainshock. The gray-scale shadows mark the ranges of three zones. **(b)** Distribution of event number along fault strike distance during three time periods. **(c)** Variation of event number with time within three zones. **(d, e)** Enlarged two time windows in (a).
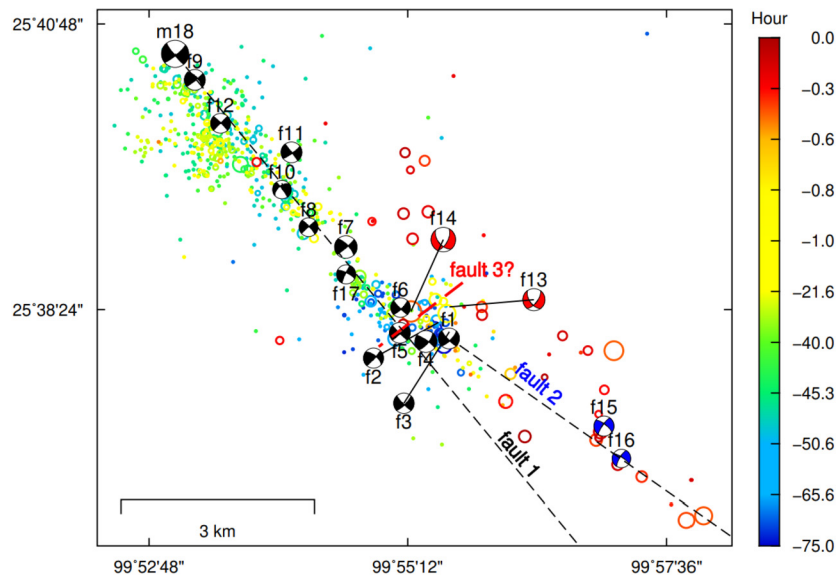

Fig. 4. The distribution of relocated foreshocks (colored by their original time relative to the M_S 6.4 mainshock) and focal mechanisms of 17 large foreshocks and the mainshock. Event IDs labeled near beach balls are corresponding to Table S1.

in Fig. 4). The largest foreshock (f14) increased the Coulomb stress by 0.5 bar at the mainshock focal location (Fig. S7), which is consistent with the result in Lei et al. (2021). The stress perturbation on the mainshock hypocenter caused by the largest foreshock is relatively small compared to the accumulated stress perturbation of other foreshocks (see next part), mainly because of the far distance. In addition, foreshocks f15 and f16 locate on a branch fault (fault 2 in Fig. 4) at the southeastern end of the main fault. It is likely that foreshocks f13, f14, f15 and f16 were located on different faults instead of the primary fault plane. We therefore considered events f1-12 and f17 to be on the main fault (fault 1) and modeled their source dimensions and static stress change to better understand the interactions between the foreshocks and mainshock hypocentre.

To explore the rupture areas of the main foreshocks and inspect how they overlap, we calculated the source patch size by assuming a circular rupture model. We started by estimating the corner frequency (f_c) from the spectrum of the seismic source for the largest foreshocks (Fig. 5), following the spectral ratio method (Onwuemeka et al., 2018; Yoon et al., 2019). The spectral ratio method is based on an empirical Green's function (EGF) approach, which uses two close earthquakes with similar waveforms, one larger (the master event) and one smaller (the EGF event). This method can cancel out non-source-related effects by taking their spectral ratio at a common station, leaving behind the source feature (Abercrombie, 2015). We first selected EGF events for each master event with a distance ≤3 km and the cross-correlation coefficient threshold of 0.5 over a time window of 2 sec before and 8 sec after *P* arrivals.
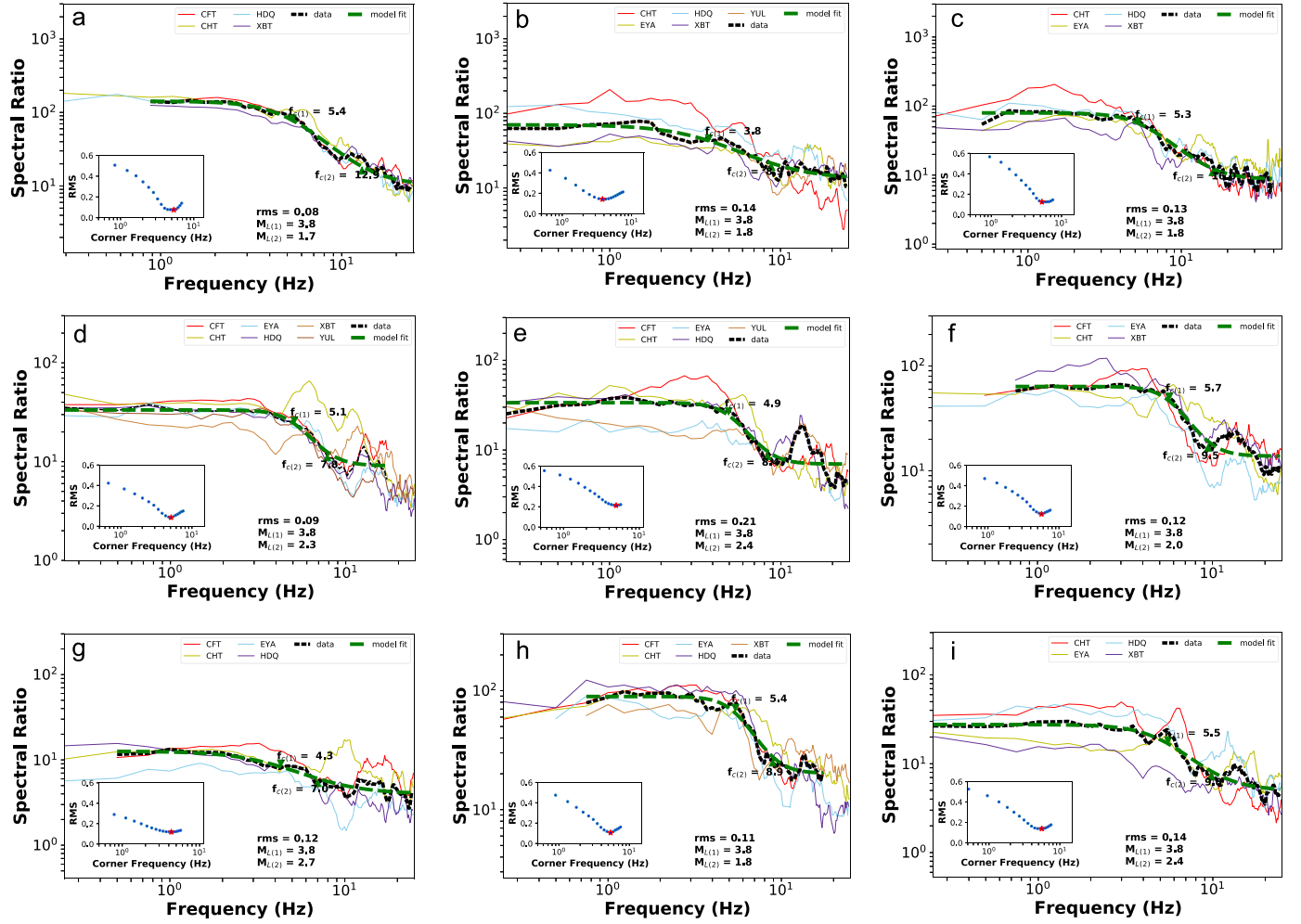
Fig. 5. Source parameter estimation for the f1 foreshock (the master event) with an EGF approach, using the spectral ratio method. Each plot has a spectral ratio estimate between the master event (f1 foreshock) and a different EGF event (smaller foreshock). Spectral ratio estimates at a given station (thin colored lines labeled by station) are used to calculate the average spectral ratio (thick black dashed line), which is fit to a Boatwright spectral model (thick green dashed line) to estimate the master event corner frequency f_{c1}, EGF event corner frequency f_{c2}.

The magnitude difference between master events and EGF events is greater than 1. At the broadband stations (Fig. 1, black triangles), we took a 3-s to 4-s time window around the S arrival to calculate the spectrum for each event. The signal-to-noise ratio (SNR) of each event was calculated using a 2-s time window for both the pre-event arrival (noise) and the S wave, and events with SNR lower than 2 were discarded. We divided the spectrum of a master event by the spectrum of an EGF event to get the spectral ratio at each station, then computed the logarithmic average spectral ratio over the stations. To estimate the corner frequencies f_c^m and f_c^e for the master and EGF events, we fitted the average spectral ratio to a Boatwright spectral model (Boatwright, 1978)

$$\Omega(f) = \frac{\Omega_0^m}{\Omega_0^e} \left[\frac{\left(1 + (f/f_c^e)^{\gamma n}\right)}{\left(1 + (f/f_c^m)^{\gamma n}\right)} \right]^{1/\gamma} \qquad (2)$$

where "m" and "e" superscripts refer to the master event and EGF event, respectively. Ω_0 is the long-period spectra amplitude, f is frequency, f_c is corner frequency, n is the spectra falloff rate, and γ is a factor that controls the sharpness of the spectrum corner. We allowed n to be determined between 2 and 3 and γ between 1 and 2 (Onwuemeka et al., 2018).

Assuming a circular crack model (Eshelby, 1957), the source radius R is given by

$$R = \frac{k\beta}{f_c} \qquad (3)$$

where f_c is corner frequency, $\beta = 3.5$ km/s for the average S wave velocity at the foreshock depth and k is a constant relating corner frequency to source dimension, depending on the particular theoretical rupture model. Since the choice of the value of k affects the estimation of stress drop, we calculated the source radius for one intermediate value, $k = 0.32$ for S waves in Sato and Hirasawa (1973) model, and two end-member rupture models ($k = 0.37$ for S waves in the Brune (1970) model, $k = 0.21$ for S waves in the Madariaga (1976) model) to represent a range of possible source dimensions (Table S1). We estimated the seismic moment (M_0) based on the magnitude (M) using the equation

$$log_{10}(M_0) = 1.5M + 9.05 \qquad (4)$$

The stress drop can be computed from the equation

$$\Delta\sigma = \frac{7}{16} \left(\frac{1}{R}\right)^3 M_0 \qquad (5)$$

Assuming the shear modulus $\mu = 30$ GPa, the average slip D is estimated by
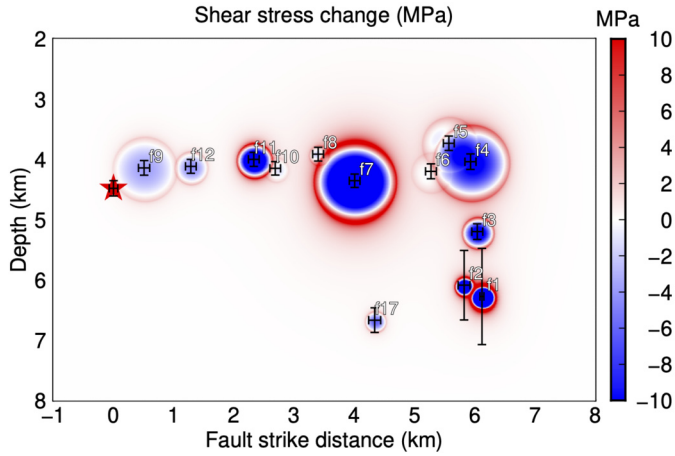
Fig. 6. Cumulative static stress change (MPa) on fault plane from thirteen largest foreshocks in time order (black-and-white beach balls in Fig. 4). The source radius is estimated assuming k = 0.32 for S waves in Sato and Hirasawa (1973) model. Event IDs are labeled near hypocenters, which is corresponding to Table S1. The red star marks the mainshock, where previous foreshocks increased the shear stress by 0.38 MPa (3.8 bar). Black bars show the location uncertainties from SVD inversion of HypoDD algorithm. Models for slip and the cumulative static stress change were from Andrews (1980) (see Method).

$$D = \frac{M_0}{\mu \pi R^2} \qquad (6)$$

We then modeled the slip within the circular fault rupture using this function from Andrews (1980):

$$d(r) = \begin{cases} D\left[1 - \left(\frac{r}{R}\right)^2\right]^{\frac{3}{2}}, & r < R \\ 0, & r > R \end{cases} \qquad (7)$$

The static shear stress changes caused by the large foreshocks were then estimated following Andrews (1980) adopting the slip function from equation (7). A model of the slip and stress change functions of an earthquake is constructed in the Fourier transform domain: taking the Fourier transform of equation (7) gets slip transform $D(k)$. Multiplying $D(k)$ by static stiffness gives the stress transform, then taking inverse Fourier transformation yields the stress field (Andrews, 1980). The shear stress decreases within the source radius of each event, and increases but decays rapidly exterior to the source.

According to the estimated source parameters under different model assumptions, most of the foreshock ruptured patches are adjacent to or only partially overlap with each other. The *Ms* 6.4 hypocenter is located outside, near the edge of the rupture zone of the foreshocks (Fig. 6 and Figs. S8-S10). Based on the Brune model, stress drops vary from 0.52 to 15.75 MPa (Table S1). Eventually the mainshock nucleates at a location where previous foreshocks have increased the shear stress by 1.01 MPa (10.1 bar) (Fig. S8). In comparison, based on the Madariaga model, stress drops vary from 2.84 to 86.12 MPa (Table S1) with a cumulative shear stress increase of 0.22 MPa (2.2 bar) at the mainshock hypocenter (Fig. S9).

Considering a large range of possible source dimensions, we took the intermediate value $k = 0.32$ in Sato and Hirasawa (1973) model as a representative, based on which the cumulative shear stress increases by 0.38 MPa (3.8 bar) at the mainshock hypocenter (Fig. 6). We also estimated the source radius by assuming a constant stress drop ($\Delta\sigma$) of 3 MPa (Dodge et al., 1996; Huang et al., 2020). The *Ms* 6.4 hypocenter is also located outside the rupture zone of the foreshocks, where the cumulative shear stress increases by 0.26 MPa (2.6 bar) at the mainshock hypocenter (Fig. S10).

6. Discussion

Several studies have suggested diverse mechanisms driving the 2021 Yangbi foreshock sequence, but the evolution of this foreshock sequence and the triggering mechanism of the mainshock is yet to be understood. For example, cascade triggering is suggested because of the lack of consistent seismicity migration toward the mainshock, few foreshocks spatially close to the mainshock (Zhang et al., 2021b), and positive stress perturbation by the largest foreshock at the *Ms* 6.4 mainshock's hypocentral region (Yang et al., 2021b). In comparison, Lei et al. (2021) suggest that the Yangbi earthquake sequence is affected by deep fluids based on active seismicity corresponding with tidal modulation. In this study, we obtain an accurate earthquake catalog during the 2021 *Ms* 6.4 Yangbi earthquake sequence. By analyzing the spatio-temporal evolution of the foreshock sequence and the relationship among source dimensions of main events, we discuss their implications for the nucleation processes of the *Ms* 6.4 earthquake.

If a pre-slip process near the nucleation zone of the mainshock controls the foreshocks, concentrated and repeated seismicity is expected during the accelerating slip (earthquake nucleation) (Fig. 7a). Numerical simulations and laboratory analogue experiments find a phase of slip acceleration preceding the mainshock dynamic rupture (earthquake nucleation) (Ampuero and Rubin, 2008; McLaskey, 2019; Ohnaka and Shen, 1999), which is supported by some observations in nature that a phase of pre-slip could accelerate into dynamic rupture (Tape et al., 2018). Companied accelerating foreshock activities before mainshocks are supported by laboratory models (Ohnaka and Shen, 1999; Scholz, 1968) and observations (Tape et al., 2018). Moreover, the localizing foreshocks near the nucleation zone are also evidenced in nature by both long-term (several years) and short-term (a few days) localization of foreshocks onto a narrower zone preceding a mainshock (Ben-Zion and Zaliapin, 2020; Savage et al., 2017). However, the 75-hour-long foreshock sequence of the *Ms* 6.4 Yangbi earthquake shows neither an accelerating nor localizing pattern with time leading up to the mainshock, which is not supportive of the pre-slip mechanism.

Except for small foreshocks, the relative location uncertainties are small compared to the largest foreshocks' source dimensions, allowing us to consider how the earthquake source patches overlap. Despite different source model assumptions (Fig. 6 and Figs. S8-S10), the source dimensions did not change too much although the stress drops vary significantly. The main large foreshocks ruptured distinct areas on the fault (Fig. 6 and Fig. S11), therefore they were unlikely to have been driven by a slow slip event (fault creep). Most foreshocks ruptured adjacent to or only partially overlapped with ruptured areas of previous events, and the *Ms* 6.4 mainshock eventually nucleated near the edge of the foreshock zone with increased shear stress. Studies of earthquake triggering elsewhere indicate that static stress change can trigger earthquakes out to several source radii (Ellsworth and Bulut, 2018; Shearer, 2012). Therefore, the adjacent ruptures may indicate either static or/and dynamic stress triggering from foreshocks to foreshocks, and then to the mainshock, which is consistent with the cascade model (Fig. 7b).

It has also been suggested that microearthquakes can be triggered by underlying physical processes, such as fluid flow (Noir et al., 1997; Chen et al., 2012) or external aseismic slip (Kato et al., 2012; Kato and Nakagawa, 2014). Increasing pore fluid pressure leads to the reduction in faults' frictional strength, which plays an important role in earthquake generation (Terakawa et al., 2012; Yoshida et al., 2017). If fluid flow is responsible for earthquake migration, the seismicity should propagate directionally with the fluid front with the migration rate decaying with time (Figs. 7c and 7d), despite a large range of diffusivities (0.01-10 m²/s) (Chen et al.,
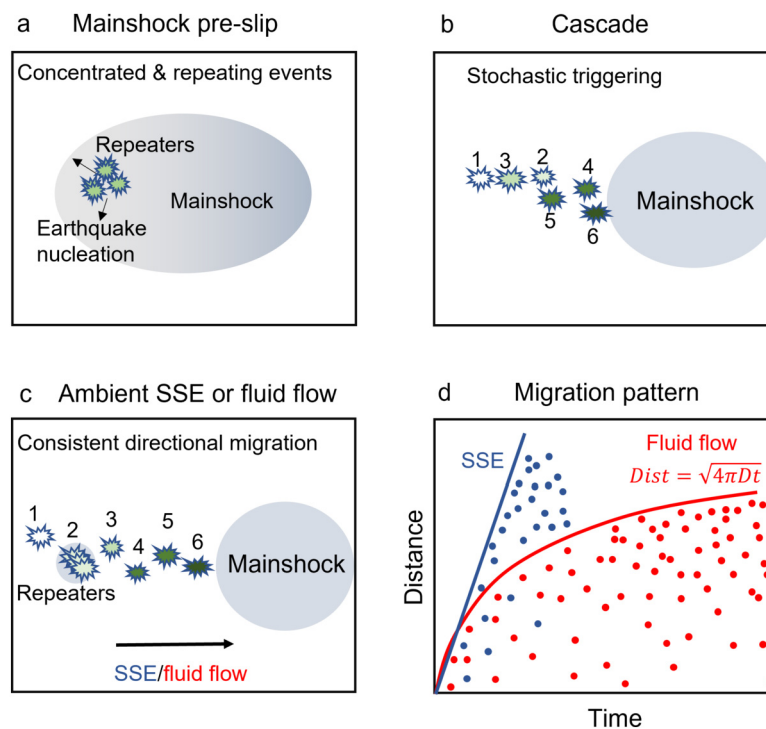
Fig. 7. Schematic diagrams for preslip (**a**), cascade triggering (**b**) and ambient slow slip event (SSE) or fluid flow (**c**). (**d**) Seismicity migration pattern if SSE (blue color)/fluid flow (red color) is the dominant driving force.

2012; Shelly et al., 2013). However, our observations of the back-and-forth spatial patterns and intermittent episodes of foreshocks are inconsistent with the fluid diffusion model.

If the foreshocks are driven by spontaneous slow slip event (fault creep) that occurred exterior to the mainshock hypocenter (Fig. 7c), the seismicity is anticipated to be characterized by repeated rupture and directional migration consistent with the slip front, and steadily increasing seismicity preceding the mainshock (Kato et al., 2012; Ruiz et al., 2014; Uchida et al., 2016). One may argue that the migration of seismicity toward the 2021 Ms 6.4 Yangbi mainshock hypocenter during the beginning of period 1 may be explained by slow slip (aseismic) propagation. A combination of aseismic transients and static stress transfer has been suggested by the observation of 2019 Mw 7.1 Ridgecrest foreshock sequence (Huang et al., 2020) and numerical simulations of slip on faults (Cattania and Segall, 2021). However, the slow-slip driving mechanism is not supported by our observations of the back-and-forth spatial patterns. Moreover, the absence of repeating foreshocks is unlikely to favor a process driven by aseismic slip (fault creep) in the foreshock period. In addition, no detectable slow slip event was reported before the Ms 6.4 mainshock dated back to 2018 on the GPS network (Fig. S12) extremely close to the fault, with 3 GPS stations within 9 km to the mainshock epicenter that were located on both sides of the fault (Zhang et al., 2021a).

Furthermore, migration behavior can also be interpreted as evidence for direct triggering between foreshocks: successive rupture of neighboring asperities, with each event nucleating at the edge of previous ones, and rare rerupture of the same asperity (as in Fig. 6). The foreshock sequence before the 1999 Izmit (Ellsworth and Bulut, 2018) and 1999 Hector Mine (Yoon et al., 2019) exhibit a cascade behavior similar to our observations in this study. Therefore, we consider that the stress perturbation of foreshocks is the primary factor triggering the mainshock, and it is not necessary to invoke slow slip to explain the observations.

An important question concerning foreshocks is why they are small and cannot evolve into a much larger rupture. Previous studies show the stress and strength on faults are heterogeneous,

therefore the magnitude of earthquakes depends on their hypocentral location, which largely determines the extent and rupture process of earthquakes (Yang et al., 2019; Yao and Yang, 2022; Yang et al., 2022a). Therefore, the foreshocks did not occur at the "right" position to potentially become the mainshock. Besides, it is intriguing to observe that the mainshock rupture swept the fault area where the foreshocks occurred, i.e. the patches of foreshocks were ruptured twice in less than 3 days. Future studies of mainshock and aftershocks using the dense seismic monitoring system (Li et al., 2021; Yang et al., 2022b) may depict potential fault branches and stress patterns on fault, which will provide a comprehensive understanding of such rerupturing on the same fault patch in a short term.

7. Conclusions

We presented a high-precision catalog of the foreshock sequence before the 2021 M_S 6.4 Yangbi mainshock based on near-field data from a local seismic network and derived the source parameters of the largest foreshocks. The spatial-temporal evolution of foreshocks is not consistent with either signature of a pre-slip nucleation process of the mainshock or slow slip and/or fluid diffusion along the mainshock ruptured fault. Rather, the 2021 Yangbi foreshock sequence can be well explained by stress triggering, particularly for those large ones occurring close to each other. The high-precision relative locations reveal that most of the large foreshocks rupture adjacent patches along the fault plane, which further suggests a cascade of stress transfer. It is not necessary to invoke aseismic slip nor high fluid pressure to explain the foreshocks and mainshock nucleation process for the Yangbi sequence.

CRediT authorship contribution statement

Gaohua Zhu: Conceptualization, Formal analysis, Methodology, Writing – original draft, Writing – review & editing. **Hongfeng Yang:** Conceptualization, Formal analysis, Funding acquisition, Writing – review & editing. **Yen Joe Tan:** Formal analysis, Funding

acquisition, Writing – review & editing. **Mingpei Jin:** Data curation. **Xiaobin Li:** Data curation. **Wei Yang:** Data curation.

Declaration of competing interest

The authors declare that they have no known competing financial interests or personal relationships that could have appeared to influence the work reported in this paper.

Data Availability Statement

Continuous data of permanent seismic stations are from China Earthquake Networks Center and Yunnan Earthquake Agency. The seismic data of temporary seismic stations are provided by Dali Center, China Seismic Experimental Site. Seismic waveform data used in this study were requested with a preauthorized account from Data Management Centre of China Seismic Network.

Acknowledgements

Appendix A. Supplementary material

Supplementary material related to this article can be found online at https://doi.org/10.1016/j.epsl.2022.117594.

References

Abercrombie, R.E., 2015. Investigating uncertainties in empirical Green's function analysis of earthquake source parameters. J. Geophys. Res., Solid Earth 120, 4263–4277. https://doi.org/10.1002/2015JB011984.

Allen, C.R., Gillespie, A.R., Yuan, H., Sieh, K.E., Buchun, Z., Chengnan, Z., 1984. Red River and associated faults, Yunnan Province, China: quaternary geology, slip rates, and seismic hazard. Geol. Soc. Am. Bull. 95 (6), 686–700. https://doi.org/10.1130/0016-7606(1984)95<686:rraafy>2.0.co;2.

Ampuero, J.-P., Rubin, A.M., 2008. Earthquake nucleation on rate and state faults – aging and slip laws. J. Geophys. Res. 113 (B1). https://doi.org/10.1029/2007jb005082.

Andrews, D.J., 1980. A stochastic fault model: 1. Static case. J. Geophys. Res., Solid Earth 85 (B7), 3867–3877. https://doi.org/10.1029/JB085iB07p03867.

Ben-Zion, Y., Zaliapin, I., 2020. Localization and coalescence of seismicity before large earthquakes. Geophys. J. Int. 223 (1), 561–583. https://doi.org/10.1093/gji/ggaa315.

Brune, J.N., 1970. Tectonic stress and the spectra of seismic shear waves from earthquakes. J. Geophys. Res. 75 (26), 4997–5009.

Boatwright, J., 1978. Detailed spectral analysis of two small New York State earthquakes. Bull. Seismol. Soc. Am. 68 (4), 1117–1131.

Bouchon, M., Durand, V., Marsan, D., Karabulut, H., Schmittbuhl, J., 2013. The long precursory phase of most large interplate earthquakes. Nat. Geosci. 6 (4), 299–302. https://doi.org/10.1038/ngeo1770.

Bouchon, M., Karabulut, H., Aktar, M., Ozalaybey, S., Schmittbuhl, J., Bouin, M.P., 2011. Extended nucleation of the 1999 Mw 7.6 Izmit earthquake. Science 331 (6019), 877–880. https://doi.org/10.1126/science.1197341.

Cattania, C., Segall, P., 2021. Precursory slow slip and foreshocks on rough faults. J. Geophys. Res., Solid Earth 126, e2020JB020430. https://doi.org/10.1029/2020JB020430.

Chen, X., Shearer, P.M., 2013. California foreshock sequences suggest aseismic triggering process. Geophys. Res. Lett. 40 (11), 2602–2607. https://doi.org/10.1002/grl.50444.

Chen, X., Shearer, P.M., Abercrombie, R.E., 2012. Spatial migration of earthquakes within seismic clusters in Southern California: evidence for fluid diffusion. J. Geophys. Res., Solid Earth 117 (B4), B04301. https://doi.org/10.1029/2011jb008973.

Dodge, D.A., Beroza, G.C., Ellsworth, W.L., 1996. Detailed observations of California foreshock sequences: implications for the earthquake initiation process. J. Geophys. Res., Solid Earth 101 (B10), 22371–22392. https://doi.org/10.1029/96JB02269.

Ellsworth, W.L., 2019. From foreshocks to mainshocks: mechanisms and implications for earthquake nucleation and rupture propagation. In: Mechanics of Earthquake Faulting, vol. 202, pp. 95–112.

Ellsworth, W.L., Bulut, F., 2018. Nucleation of the 1999 Izmit earthquake by a triggered cascade of foreshocks. Nat. Geosci. 11 (7), 531–535. https://doi.org/10.1038/s41561-018-0145-1.

Eshelby, J.D., 1957. The determination of the elastic field of an ellipsoidal inclusion, and related problems. Proc. R. Soc. Lond. A 241 (1226), 376–396.

Gomberg, J., 2018. Unsettled earthquake nucleation. Nat. Geosci. 11 (7), 463–464. https://doi.org/10.1038/s41561-018-0149-x.

Guo, R., Yang, H., et al., 2022. Rupture imaging of the 2021 Ms 6.4 Yangbi, China, earthquake: an event sequence occurring on a blind fault, in preparation.

Hardebeck, J.L., Shearer, P.M., 2002. A new method for determining first-motion focal mechanisms. Bull. Seismol. Soc. Am. 92 (6), 2264–2276. https://doi.org/10.1785/0120010200.

Huang, H., Meng, L., Bürgmann, R., Wang, W., Wang, K., 2020. Spatio-temporal foreshock evolution of the 2019 M 6.4 and M 7.1 Ridgecrest, California earthquakes. Earth Planet. Sci. Lett. 551, 116582. https://doi.org/10.1016/j.epsl.2020.116582.

Kato, A., Ben-Zion, Y., 2020. The generation of large earthquakes. Nat. Rev. Earth Environ. 2 (1), 26–39. https://doi.org/10.1038/s43017-020-00108-w.

Kato, A., Nakagawa, S., 2014. Multiple slow-slip events during a foreshock sequence of the 2014 Iquique, Chile Mw 8.1 earthquake. Geophys. Res. Lett. 41 (15), 5420–5427. https://doi.org/10.1002/2014GL061138.

Kato, A., Obara, K., Igarashi, T., Tsuruoka, H., Nakagawa, S., Hirata, N., 2012. Propagation of slow slip leading up to the 2011 Mw 9.0 Tohoku-Oki earthquake. Science 335 (6069), 705–708. https://doi.org/10.1126/science.1215141.

Kato, A., Fukuda, J., Nakagawa, S., Obara, K., 2016. Foreshock migration preceding the 2016 Mw 7.0 Kumamoto earthquake, Japan. Geophys. Res. Lett. 43, 8945–8953. https://doi.org/10.1002/2016GL070079.

Klein, F.W., 2002. User's guide to HYPOINVERSE-2000, a Fortran program to solve for earthquake locations and magnitudes. Report Rep. 2002-171, 123 pp.

Lei, X.L., Wang, Z.W., Ma, S.L., He, C.R., 2021. A preliminary study on the characteristics and mechanism of the May 2021 M_S 6.4, Yangbi earthquake sequence, Yunna, China. Acta Seismol. Sin. 43 (3), 1–24. https://doi.org/10.11939/jass.20210100 (in Chinese).

Li, J., Yao, H., Wang, B., Yang, Y., Hu, X., Zhang, L., Ye, B., Yang, J., Li, X., Liu, F., Chen, G., Guo, C., Yang, W., 2021. A real-time AI-assisted seismic monitoring system based on new nodal stations with 4G telemetry and its application in the Yangbi MS 6.4 aftershock monitoring in southwest China. Earthq. Res. Adv. (ISSN 2772-4670) 100033. https://doi.org/10.1016/j.eqrea.2021.100033.

Liu, C., Yang, H., Wang, B., Yang, J., 2021. Impacts of reservoir water level fluctuation on measuring seasonal seismic travel time changes in the Binchuan basin, Yunnan, China. Remote Sens. 13, 2421. https://doi.org/10.3390/rs13122421.

Luan, Y., Yang, H., Wang, B., Yang, W., Wang, W., Yang, J., Li, X., 2022. Time-lapse monitoring of daily velocity changes in Binchuan, southwestern China, using large volume air gun source array data. Seismol. Res. Lett. 93 (2A), 914–930. https://doi.org/10.1785/0220210160.

Madariaga, R., 1976. Dynamics of an expanding circular fault. Bull. Seismol. Soc. Am. 66 (3), 639–666.

McLaskey, G.C., 2019. Earthquake initiation from laboratory observations and implications for foreshocks. J. Geophys. Res., Solid Earth 124 (12), 12882–12904. https://doi.org/10.1029/2019jb018363.

Mori, J., 1996. Rupture directivity and slip distribution of the M 4.3 foreshock to the 1992 Joshua Tree earthquake, Southern California. Bull. Seismol. Soc. Am. 86 (3), 805–810. https://doi.org/10.1785/bssa0860030805.

Mousavi, S.M., Ellsworth, W.L., Zhu, W., Chuang, L.Y., Beroza, G.C., 2020. Earthquake transformer-an attentive deep-learning model for simultaneous earthquake detection and phase picking. Nat. Commun. 11 (1), 3952. https://doi.org/10.1038/s41467-020-17591-w.

Noir, J., Jacques, E., Békri, S., Adler, P.M., Tapponnier, P., King, G.C.P., 1997. Fluid flow triggered migration of events in the 1989 Dobi Earthquake sequence of central Afar. Geophys. Res. Lett. 24 (18), 2335–2338. https://doi.org/10.1029/97gl02182.

Ohnaka, M., Shen, L.-f., 1999. Scaling of the shear rupture process from nucleation to dynamic propagation: implications of geometric irregularity of the rupturing surfaces. J. Geophys. Res., Solid Earth 104 (B1), 817–844. https://doi.org/10.1029/1998jb900007.

Onwuemeka, J., Liu, Y., Harrington, R.M., 2018. Earthquake stress drop in the Charlevoix Seismic Zone, eastern Canada. Geophys. Res. Lett. 45, 12,226–12,235. https://doi.org/10.1029/2018GL079382.

Peng, Z., Zhao, P., 2009. Migration of early aftershocks following the 2004 Parkfield earthquake. Nat. Geosci. 2, 877. https://doi.org/10.1038/ngeo697.

Rubin, A.M., Ampuero, J.-P., 2005. Earthquake nucleation on (aging) rate and state faults. J. Geophys. Res. 110, B11312. https://doi.org/10.1029/2005JB003686.

Ruiz, S., Metois, M., Fuenzalida, A., Ruiz, J., Leyton, F., Grandin, R., Vigny, C., Madariaga, R., Campos, J., 2014. Intense foreshocks and a slow slip event preceded the 2014 Iquique Mw 8.1 earthquake. Science 345 (6201), 1165–1169. https://doi.org/10.1126/science.1256074.

Sato, T., Hirasawa, T., 1973. Body wave spectra from propagating shear cracks. J. Phys. Earth 21 (4), 415–431. https://doi.org/10.4294/jpe1952.21.415.

Savage, H.M., Keranen, K.M., Schaff, D.P., Dieck, C., 2017. Possible precursory signals in damage zone foreshocks. Geophys. Res. Lett. 44 (11), 5411–5417. https://doi.org/10.1002/2017gl073226.

Scholz, C.H., 1968. Experimental study of the fracturing process in brittle rock. J. Geophys. Res. 73 (4), 1447–1454. https://doi.org/10.1029/JB073i004p01447.

Shearer, P.M., 2012. Space-time clustering of seismicity in California and the distance dependence of earthquake triggering. J. Geophys. Res., Solid Earth 117 (B10). https://doi.org/10.1029/2012jb009471.

Shelly, D.R., Hill, D.P., Massin, F., Farrell, J., Smith, R.B., Taira, T.a., 2013. A fluid-driven earthquake swarm on the margin of the Yellowstone caldera. J. Geophys. Res., Solid Earth 118 (9), 4872–4886. https://doi.org/10.1002/jgrb.50362.

Shen, Z.K., Lü, J., Wang, M., Bürgmann, R., 2005. Contemporary crustal deformation around the southeast borderland of the Tibetan Plateau. J. Geophys. Res., Solid Earth 110, B11409.

Shen, Z.K., Sun, J., Zhang, P., Wan, Y., Wang, M., Burgmann, R., et al., 2009. Slip maxima at fault junctions and rupturing of barriers during the 2008 Wenchuan earthquake. Nat. Geosci. 2 (10), 718–724.

Shi, X., Sieh, K., Weldon, R., Zhu, C., Han, Y., Yang, J., Robinson, S.W., 2018. Slip rate and rare large prehistoric earthquakes of the Red River fault, Southwestern China. Geochem. Geophys. Geosyst. 19 (7), 2014–2031. https://doi.org/10.1029/2017GC007420.

Su, J., Liu, M., Zhang, Y., Wang, W., Li, H., Yang, J., Li, X., Zhang, M., 2021. High resolution earthquake catalog building for the 21 May 2021 Yangbi, Yunnan, *Ms* 6.4 earthquake sequence using deep-learning phase picker. Chin. J. Geophys. 64 (8), 2647–2656. https://doi.org/10.6038/cjg2021O0530.

Tape, C., Holtkamp, S., Silwal, V., Hawthorne, J., Kaneko, Y., Ampuero, J.P., Ji, C., Ruppert, N., Smith, K., West, M.E., 2018. Earthquake nucleation and fault slip complexity in the lower crust of central Alaska. Nat. Geosci. 11 (7), 536–541. https://doi.org/10.1038/s41561-018-0144-2.

Terakawa, T., Miller, S.A., Deichmann, N., 2012. High fluid pressure and triggered earthquakes in the enhanced geothermal system in Basel, Switzerland. J. Geophys. Res. 117, B07305. https://doi.org/10.1029/2011JB008980.

Uchida, N., Iinuma, T., Nadeau, R.M., Bürgmann, R., Hino, R., 2016. Periodic slow slip triggers megathrust zone earthquakes in northeastern Japan. Science 351 (6272), 488–492. https://doi.org/10.1126/science.aad3108.

Waldhauser, F., Ellsworth, W.L., 2000. A Double-difference earthquake location algorithm: method and application to the Northern Hayward fault, California. Bull. Seismol. Soc. Am. 90 (6), 1353–1368. https://doi.org/10.1785/0120000006.

Wang, B., Ge, H., Yang, W., Wang, W., Wang, B., Wu, G.-d., Su, Y.-j., 2012. Transmitting seismic station monitors fault zone at depth. Eos Trans. AGU 93, 49–50. https://doi.org/10.1029/2012EO050001.

Wang, Y.Z., et al., 2008. GPS-constrained inversion of present-day slip rates along major faults of the Sichuan-Yunnan region. Sci. China, Ser. D, Earth Sci. 51 (9), 1267–1283. https://doi.org/10.1007/s11430-008-0106-4.

Yao, S., Yang, H., 2022. Hypocentral dependent shallow slip distribution and rupture extents along a strike-slip fault. In: Earth and Planetary Science Letters.

Yang, H., Zhu, L., Chu, R., 2009. Fault-plane determination of the 18 April 2008 Mount Carmel, Illinois, earthquake by detecting and relocating aftershocks. Bull. Seismol. Soc. Am. 99 (6), 3413–3420. https://doi.org/10.1785/0120090038.

Yang, H., Yao, S., He, B., Newman, A., 2019. Earthquake rupture dependence on hypocentral locations along the Nicoya Peninsula subduction megathrust. Earth Planet. Sci. Lett. https://doi.org/10.1016/j.epsl.2019.05.030.

Yang, H., Duan, Y., Song, J., Jiang, X., Tian, X., Yang, W., et al., 2020. Fine structure of the Chenghai fault zone, Yunnan, China, constrained from teleseismic travel time and ambient noise tomography. J. Geophys. Res., Solid Earth 125, e2020JB019565. https://doi.org/10.1029/2020JB019565.

Yang, H., Duan, Y., Song, J., Yang, W., Wang, W., Tian, X., Wang, B., 2021a. Illuminating high-resolution crustal fault zones and temporal changes using multi-scale dense arrays and airgun sources. Earthq. Res. Adv. 1 (1). https://doi.org/10.1016/j.eqrea.2021.100001.

Yang, T., et al., 2021b. Relocation of the foreshocks and aftershocks of the 2021 *Ms* 6.4 Yangbi earthquake sequence, Yunnan, China. J. Earth Sci. https://doi.org/10.1007/s12583-021-1527-7.

Yang, H., Yao, S., Chen, X., 2022a. Rupture propagation on heterogeneous fault: challenges for predicting earthquake magnitude. Chin. Sci. Bull. https://doi.org/10.1360/TB-2021-1086.

Yang, H., Wang, D., Guo, R., Xie, M., Zang, Y., Wang, Y., Yao, Q., Cheng, C., An, Y., Zhang, Y., 2022b. Rapid report of the 8 January 2022 Menyuan Ms 6.9 earthquake, Qinghai, China. Earthq. Res. Adv. https://doi.org/10.1016/j.eqrea.2022.100113.

Yoshida, K., Saito, T., Urata, Y., Asano, Y., Hasegawa, A., 2017. Temporal changes in stress drop, frictional strength, and earthquake size distribution in the 2011 Yamagata-Fukushima, NE Japan, earthquake swarm, caused by fluid migration. J. Geophys. Res., Solid Earth 122, 10,379–10,397. https://doi.org/10.1002/2017JB014334.

Yoon, C.E., Yoshimitsu, N., Ellsworth, W.L., Beroza, G.C., 2019. Foreshocks and mainshock nucleation of the 1999 Mw 7.1 Hector Mine, California, Earthquake. J. Geophys. Res., Solid Earth 124 (2), 1569–1582. https://doi.org/10.1029/2018jb016383.

Zhang, M., Ellsworth, W.L., Beroza, G.C., 2019. Rapid earthquake association and location. Seismol. Res. Lett. 90 (6), 2276–2284. https://doi.org/10.1785/0220190052.

Zhang, K., Gan, W., Liang, S., et al., 2021a. Coseismic displacement and slip distribution of the 2021 May 21, *Ms* 6.4, Yangbi Earthquake derived from GNSS observations. Chin. J. Geophys. 64 (7), 2253–2266. https://doi.org/10.6038/cjg2021O0524 (in Chinese).

Zhang, Y., An, Y., Long, F., Zhu, G., Qin, M., Zhong, Y., Xu, Q., Yang, H., 2021b. Short-term foreshock and aftershock patterns of the 2021 *Ms* 6.4 Yangbi earthquake sequence. Seismol. Res. Lett. https://doi.org/10.1785/0220210154.

Zhu, G., Yang, H., Lin, J., Zhou, Z., Xu, M., Sun, J., Wan, K., 2019. Along-strike variation in slab geometry at the southern Mariana subduction zone revealed by seismicity through ocean bottom seismic experiments. Geophys. J. Int. 218 (3), 2122–2135. https://doi.org/10.1093/gji/ggz272.